Structural Engineering and Mechanics, Vol. 38, No. 4 (2011) 479-501
DOI: http://dx.doi.org/10.12989/sem.2011.38.4.479

Debonding failure analysis of FRP-retrofitted concrete panel under blast loading

Ho Jin Kim[1a], Na Hyun Yi[2b], Sung Bae Kim[2c], Jin Won Nam[3d], Ju Hyung Ha[2,4e] and Jang-Ho Jay Kim*[2]

[1]*Civil Engineering Research Institute, ATMACS Co. Ltd., Sungnam 463-760, Korea*
[2]*School of Civil and Environmental Engineering, Yonsei University, Concrete Structural Engineering Laboratory, Seoul 120-794, Korea*
[3]*Department of Civil & Environmental Engineering, Southern University, Suite 321, Pinchback Building, Baton Rouge, LA, 70813, USA*
[4]*Material Division, Hyundai Institute of Construction Technology, Yongin-si, Gyunggi-do 446-716, Korea*

(Received April 22, 2010, Accepted March 9, 2011)

Abstract. Even though fiber reinforced polymer (FRP) has been widely used as a retrofitting material, the FRP behavior and effect in FRP retrofitted structure under blast loading, impulsive loading with instantaneous time duration, has not been accurately examined. The past studies have focused on the performance of FRP retrofitted structures by making simplifications in modeling, without incorporating accurate failure mechanisms of FRP. Therefore, it is critical to establish an analytical model that can properly consider the specific features of FRP material in evaluating the response of retrofitted concrete structures under blast loading. In this study, debonding failure analysis technique for FRP retrofitted concrete structure under blast loading is suggested by considering FRP material characteristics and debonding failure mechanisms as well as rate dependent failure mechanism based on a blast resisting design concept. In addition, blast simulation of FRP retrofitted RC panel is performed to validate the proposed model and analysis method. For validation of the proposed model and analysis method, the reported experimental results are compared with the debonding failure analysis results. From the comparative verification, it is confirmed that the proposed analytical model considering debonding failure of FRP is able to reasonably predict the behavior of FRP retrofitted concrete panel under blast loading.

Keywords: fiber reinforced polymer; KFRP; AFRP; GFRP; CFRP; retrofitting material; blast load; failure mechanism; rate dependent; debonding failure.

1. Introduction

Recently, FRP has been increasingly used for strengthening RC structures in civil and

*Corresponding author, Associate Professor, E-mail: jjhkim@yonsei.ac.kr
[a]Ph.D., Manager
[b]Doctoral Student
[c]Ph.D., Researcher
[d]Adjunct Professor
[e]Doctoral Student, Chief Engineer

architectural structural engineering fields (Chen and Teng 2001, Matta *et al.* 2005, Takakshi 2009, Mahini and Ronagh 2009, Dai *et al*. 2008, Dogan and Anil 2010). Especially, to enhance the energy-absorbing capacity of the structures to resist extreme loading such as impact and blast loads, fiber reinforced polymer (FRP) retrofit method has been the most widely used construction method in the world (Buchan and Chen 2007). In blast loading condition, FRP retrofit effectiveness should not only consider stiffness and energy absorption enhancements, but also the effect of catching debris (debris catching capability) from the short wave applied by a blast load (Nam *et al*. 2009, Mosalam and Mosallam 2001, Lu 2009, Gong *et al*. 2009, Cho 2009, Kumar 2010). However, the current in-depth knowledge about fundamental behavior of FRP strengthened structures under blast loading is insufficient to perform a detailed analysis and design for structural retrofitting. For example, even though the debonding failure of FRP between FRP and concrete has been commonly reported from numerous blast field tests, most of the studies have focused on the overall performance of FRP retrofitted structures by simplified FRP modeling without accurately applying the material characteristics and failure mechanisms of FRP. If the effect of material characteristics and failure mechanisms are not accurately incorporated, the retrofit design and performance evaluation of FRP retrofitted concrete structures may become inaccurate for extremely high loading rate cases (Dai and Yokota 2008, Zhou *et al*. 2007, Thiruppukuzhi and Sun 2001). Therefore, the consideration of the strain rate effect and debonding failure of FRP might be the most significant requirements in blast analysis of FRP retrofitted concrete structures. In this study, the dynamic bond model that can consider the debonding failure behavior is developed based on the Lorenzis and Tegola's (2005) simple approach. Also, the debonding failure model is implemented in blast simulations using contact interface modeling in finite element analysis.

The strain rate effect of concrete and steel material models have been considered in numerous analytical studies (Nam *et al*. 2010, Al-Hassini and Kaddour 1998, Kim and Fries 2002, Kotsovos *et al*. 2008, Pandey 2010, Valipour *et al*. 2009, Yun *et al*. 2008, Ngo and Mendis 2009). However, these constitutive models of concrete and steel are developed without properly incorporating the strain rate effect of FRP as a damage energy absorption model for high strain rate condition. From the study by Park (2003), the failure mechanisms and strengths of FRP are found to be strongly dependent on the strain rate. Therefore, in the Lorenzis and Tegola's model (2005), several new strength terms related to strain rate of FRP failure mechanism are defined to represent the interaction of stresses in orthogonal plane directions. In Hashin's (1980) failure criteria for uni-directional fiber composites, uni-directional fiber composite are assumed to be transversely isotropic with respect to their fiber direction since the fibers are randomly placed. Chang and Chang (1987) presented a progressive damage model for laminated composite subjected to static loading where a set of failure criteria and material property degradation models corresponding to each failure criterion was provided. The failure model is in a simple form by setting the transverse modulus and Poisson's ratio to be zero.

Experimental works have been carried out to investigate the strain rate effect on the constitutive and strength behaviors of FRPs. Al-Salehi *et al*. (1989) conducted experiments for the strain rate effect on the strength of ply angle of glass fiber reinforced epoxy resin polymer (GFRP) tubes under high loading rate condition, which showed that a substantial increase in strength occurs under high strain rate condition. Al-Hassani and Kaddour (1998) performed a comprehensive experimental research on the strain rate effect on the in-plane mechanical properties of continuous Kevlar, Aramid, glass, and carbon fiber reinforced polymers (KFRP, AFRP, GFRP, and CFRP). The research work concentrated on the indirect determination of uni-directional dynamic properties from

the behavior of laminate angles by means of an extraction process. The results showed a high dependency of longitudinal, transverse, and in-plane shear strengths as well as transverse modulus on the strain rate.

Meanwhile, many studies have been carried out on behavior predictions and experimental evaluations on FRP retrofitted concrete structures. Landry (2003) has experimentally and analytically evaluated the protective performance of concrete masonry walls; Morrill *et al*. (2001) conducted a blast field test on reinforced concrete (RC) columns and walls retrofitted with FRP, and compared their test results to the finite element analysis results. Malvar *et al*. (2004) developed a numerical model for RC columns surface wrapped by AFRP, GFRP, and CFRP for the comparison of the analytical results to experimental data. Their study results proved that retrofitting a column with FRP jacket effectively preserves the structural capacity of the structure under earthquake or blast loading. Furthermore, Davidson *et al*. (2005) performed an explosive test on a masonry wall retrofitted by elasto-plastic polymer material, and to simulate compared their test results by finite element analysis. In the finite element analysis, the material properties of the elasto-plastic polymer and the strain rate effect on blast load are considered. Pham (2002) used explicit time integration to obtain a finite element equation of the behavior of a GFRP tube under an impact load to model GFRP using two-dimensional shell elements with orthotropic elastic material.

Based on the literature review of the previous works, the progressive failure mechanism and material property degradation are the main strain rate effect of FRP during deformation under blast loading. Accordingly, a comprehensive analytical FRP model including the strain rate effect and debonding behavior need to be developed to precisely analyze FRP retrofitted concrete structures under blast loading.

2. FRP rate dependent failure model

A common assumption used in FRP constitutive modeling is that FRP is a linear elastic material until it reaches its tensile strength. Even when a very high loading rate condition such as a blast load is applied, it is commonly assumed that FRP is a linear elastic material in conventional and classical modeling. Therefore, most FRP models ignore the strain rate effect and progressive failure modes of FRP. However, except when the load is applied in the fiber direction, FRP composites exhibit nonlinear and rate dependent behavior (Thiruppukuzhi and Sun 2001). This behavior has been reported previously where the strain rate effect and progressive failure modes of FRPs strongly exist under blast loading (Park *et al*. 2006).

In this study, a methodology is developed to consider the strain rate effect on the failure mode of FRP to accurately predict the dynamic response of FRP retrofitted concrete structures under high-explosive blast loading. The failure modes in the proposed FRP model for uni-directional ply and woven ply include fiber breakage and matrix cracking failures. The proposed FRP failure model is implemented into its stiffness matrix to describe the material degradation characteristic of the damage region by using Park's model. Also, the proposed model's failure criteria include the strain rate effect on material strength previously reported from various experimental studies.

2.1 Proposed FRP failure model without strain rate effect

Failure of FRP composites are caused by either fiber buckling, fiber breakage, matrix cracking,

delamination, or by a combination of these failure modes as shown in Fig. 1. Therefore, a FRP failure model must be able to consider these failure mechanisms. Although various FRP failure models have been proposed in the past (Gibson 1994, Swanson 1997, Lenwari *et al*. 2002, Yi *et al.* 2009), no model has been sufficiently developed to the level of application in practical engineering design.

The failure model of FRP proposed in this study is based on the progressive failure criterion of Hashin (1980) and the Chang and Chang's model (1987). For relatively thick FRPs undergoing bending deformation under transverse pressure loading, the effect of delamination on the structural response can be ignored since the fiber breakage failure is predominantly responsible for the structural failure. The property degradation is dependent upon the failure mechanism due to the damages. Therefore, the proposed failure model of FRP is implemented into its stiffness matrix to reflect the material property degradation characteristic by using Park's model. The quadratic failure surface concept of the failure model developed in this study is shown in Fig. 2.

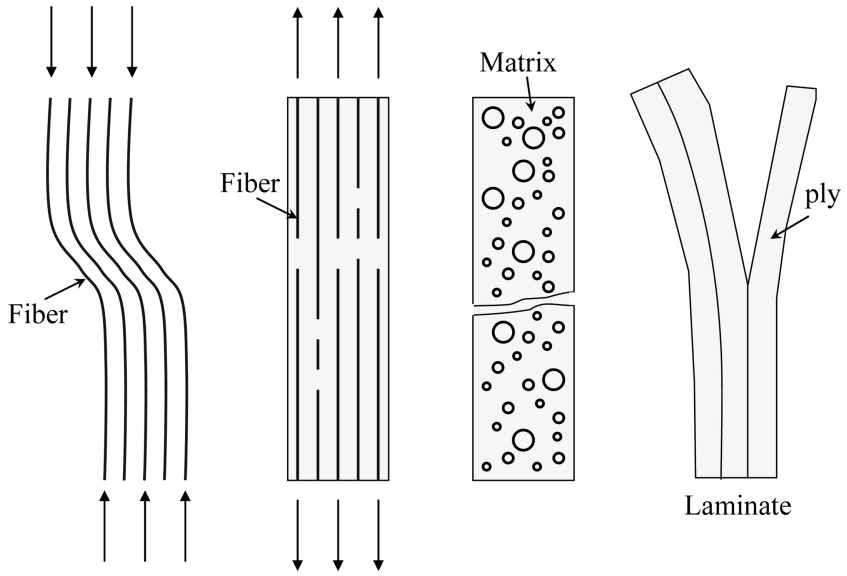

Fig. 1 Typical failure modes of FRP composites (Kollár and Springer 2002)

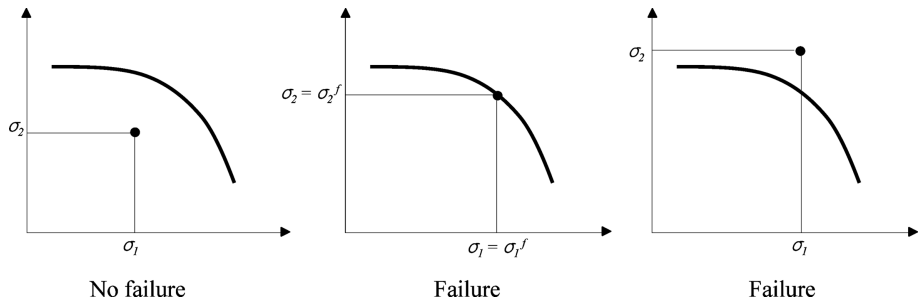

Fig. 2 Representation of the quadratic failure surface (Kollár and Springer 2002)

Table 1 Failure criterion of uni-directional FRP and bi-directional FRP

Uni-directional FRP	Matrix cracking failure	Tension $e_m = \left(\frac{\sigma_{22}}{Y_t}\right)^2 + \left(\frac{\tau_{12}}{SC_{12}}\right)^2 \geq 1$ for $\sigma_{22} > 0$	(1)
		Compression $e_m = \frac{\sigma_{22}}{Y_c}\left[\left(\frac{Y_c}{2SC_{23}}\right)^2 - 1\right] + \left(\frac{\sigma_{22}}{2SC_{23}}\right)^2 + \left(\frac{\tau_{12}}{SC_{12}}\right)^2 \geq 1$, for $\sigma_{22} < 0$	(2)
		In-plane elastic stiffness $C_E = \begin{bmatrix} v_f E_f & 0 & 0 \\ 0 & mdC_{22} & 0 \\ 0 & 0 & 0 \end{bmatrix}$	(3)
	Fiber breakage failure	Tension $e_f = \left(\frac{\sigma_{11}}{X_t}\right)^2 + \left(\frac{\tau_{12}}{SC_{12}}\right)^2 \geq 1$ for $\sigma_{11} > 0$	(4)
		Compression $e_f = \left(\frac{\sigma_{11}}{X_c}\right)^2 \geq 1$ for $\sigma_{11} < 0$	(5)
		In-plane elastic stiffness $C_E = \begin{bmatrix} \frac{v_m E_m}{1-(v_{12}^m)^2} & \frac{v_m v_{12}^m E_m}{1-(v_{12}^m)^2} & 0 \\ \frac{v_m v_{12}^m E_m}{1-(v_{12}^m)^2} & \frac{v_m E_m}{1-v_{12}v_{21}} & 0 \\ 0 & 0 & v_m G_m \end{bmatrix} = \begin{bmatrix} mdC_{11} & 0 & 0 \\ 0 & mdC_{22} & 0 \\ 0 & 0 & mdG_{12} \end{bmatrix}$	(6)
Bi-directional FRP	Fiber breakage failure in the fill direction	Tension $e = \left(\frac{\sigma_{22}}{X_t}\right)^2 + \left(\frac{\tau_{12}}{SC_{12}}\right)^2 \geq 1$ and $\left(\frac{\sigma_{22}}{X_t}\right)^2 \geq \left(\frac{\tau_{12}}{SC_{12}}\right)^2$ for $\sigma_{22} > 0$	(7)
		Compression $e = \left(\frac{\sigma_{22}}{X_c}\right)^2 \geq 1$ for $\sigma_{22} < 0$	(8)
		In-plane elastic stiffness $C_E = \begin{bmatrix} E_1 & 0 & 0 \\ 0 & mdC_{22} & 0 \\ 0 & 0 & 0 \end{bmatrix}$	(9)
	Fiber breakage failure in the warp direction	Tension $e = \left(\frac{\sigma_{11}}{X_t}\right)^2 + \left(\frac{\tau_{12}}{SC_{12}}\right)^2 \geq 1$ and $\left(\frac{\sigma_{11}}{X_t}\right)^2 \geq \left(\frac{\tau_{12}}{SC_{12}}\right)^2$ for $\sigma_{11} > 0$	(10)
		Compression $e = \left(\frac{\sigma_{11}}{X_c}\right)^2 \geq 1$ for $\sigma_{11} < 0$	(11)
		In-plane elastic stiffness $C_E = \begin{bmatrix} mdC_{11} & 0 & 0 \\ 0 & E_2 & 0 \\ 0 & 0 & G_{12} \end{bmatrix}$	(12)

The uni-directional FRP failure criteria of matrix cracking and fiber breakage are shown as Eqs. (1)-(4) in Table 1. And, for bi-directional FRPs such as woven composites, the two perpendicular fiber breakages are the main failure mechanism. In this study, the failure criteria proposed by Park *et al*. (2006) and Chang and Chang (1987) are modified to represent the failure mechanisms of bi-directional FRPs. The proposed bi-directional failure criteria are shown as Eqs. (5)-(8) in Table 1. The parameters used in the failure criteria shown in Table 1 are as follows. σ_{11} and σ_{22} are normal stresses in x- and y-direction, respectively; τ_{12} is shear stress in xy-direction; SC_{12} is an in-plane shear strength; SC_{23} is a transverse shear strength; X_t and X_c are tensile and compression strengths, respectively; Y_c is a compressive strength in transverse direction; e is a failure index representing the combined effect of normal and shear stresses; e_m and e_f are the failure indices for matrix cracking and fiber breakage failure modes, respectively; v_f and v_m are a fiber and matrix volume fraction, respectively; v_{12}^m is the Poisson's ratio of matrix; E_f and E_m are a longitudinal Young's modulus of the fiber and matrix, respectively; G_m is a shear modulus of the matrix; *md* is a constant representing the material property degradation. Also, C_{11} and C_{22} are the 1st and 2nd row and column entry of the intact in-plane elastic stiffness matrix, respectively (Park 2003). For fiber breakage failure, it is assumed that the fibers are completely broken and the failed region becomes an isotropic material composed only of epoxy matrix. The failure index with a value of over 1 is considered as a failed material.

2.2 Analytical example of the proposed failure model

To assess the FRP failure model, dynamic analysis has been conducted for a square composite plate with all edges clamped with the FRP model either as failure or non-failure model as shown in Fig. 3. The composite plate is subjected to a uniform blast pressure over the top surface. The application of the FRP failure model in finite element analysis is performed using a commercial explicit analysis program LS-DYNA version 971. The FRP chosen for the application is S2-Glass/ 8552 (GFRP) and the material properties reported by Thiruppukuzhi and Sun (2001) are used as shown in Table 2 of quasi-static part.

The maximum in-plane stress distributions of the non-failure and failure model analyses are shown in Fig. 4. In the failure model analysis, the failure propagation started at the edges as shown

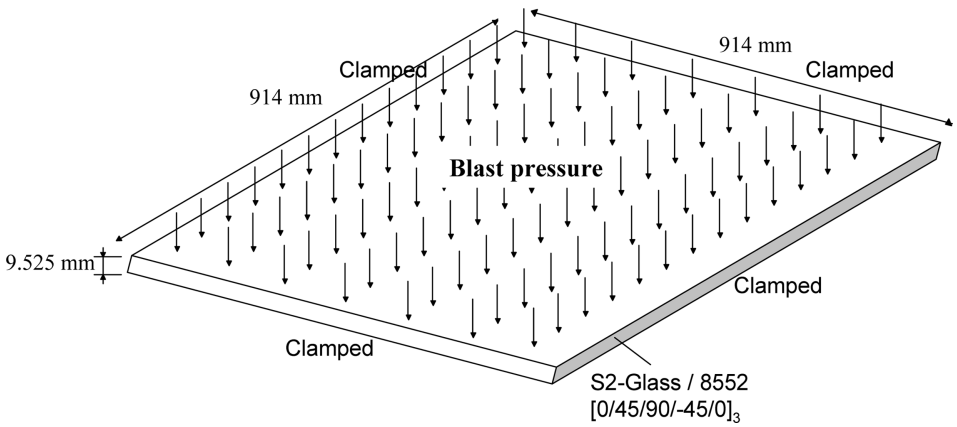

Fig. 3 Schematic configuration of the square FRP plate under blast loading

Table 2 Material properties of FRP model (Park *et al*. 2006)

Material properties	Quasi-static	Dynamic with strain rate effect
Longitudinal modulus, E_x (GPa)	28.3	28.3
Transverse modulus, E_y (GPa)	28.3	28.3
Shear modulus, G_{xy} (GPa)	5.86	5.86
Poisson's ratio, ν_{xy}	0.23	0.23
Quasi-static longitudinal tensile strength, X_t (MPa)	534.96	$48.16\log\dot{\varepsilon}_{11}+727.6$
Quasi-static longitudinal compressive strength, X_c (MPa)	345.00	$48.16\log\dot{\varepsilon}_{11}+486.6$
Quasi-static transverse tensile strength, Y_t (MPa)	534.96	$48.16\log\dot{\varepsilon}_{22}+727.6$
Quasi-static transverse compressive strength, Y_c (MPa)	345.00	$48.16\log\dot{\varepsilon}_{22}+486.6$
Quasi-static in-plane shear strength, SC (MPa)	86.98	$8.08\log\dot{\varepsilon}_{12}+119.3$
Density, ρ (kg/m^3)	1,800	1,800

in Fig. 4(b) where the failure is governed by matrix cracking as shown in Fig. 4(a). The failed region propagated toward the plate center and along the edges until the fiber breakage occurred at the center.

A comparison of the analysis results using the failure and non-failure models is shown in Fig. 5. In the non-failure model analysis, the maximum displacement at the FRP plate center is approximately 77 mm at the time of 1.3 msec followed by an elastic recovery. For the failure model analysis, the maximum displacement is approximately 94 mm at the time of 1.54 msec, which is larger than the non-failure model displacement. However, as shown in Fig. 4(b) and Fig. 5, the center of FRP plate has collapsed due to its stresses exceeding the failure stress criterion of FRP. The collapsed state is represented not only as a structural failure of FRP plate but also as a divergence in the analysis results due to element elimination. Therefore, the developed failure FRP model can be effectively implemented into finite element analysis and predict the non-linear failure behavior of FRP plate under blast loading.

2.3 Proposed FRP failure model with strain rate effect

Recently, many studies have focused on the topic of strain rate effect of concrete and reinforcing steel under blast or impact loading (Malvar *et al*. 1997, Malvar *et al*. 2004, Nam *et al*. 2010, Ngo and Mendis 2009, Guzas and Earls 2010). However, a representative strain rate effect included FRP model has not been developed for blast analysis. Therefore, in this study, a FRP failure model with strain rate effect is proposed based on in-plane material strengths. From the literature review, it was found that strain rate does not and does affect FRP's elastic and plastic behavior, respectively (Thiruppukuzhi and Sun 2001). Therefore, an elastic-viscoplastic model is needed to consider such behavior where a plastic potential function is required to characterize the plastic deformation at any given strain rate. Therefore, the strain rate dependent failure criterion in this study is based on viscoplastic strain as shown in Fig. 6. The rate dependent parameters of viscoplastic behavior are frequently obtained by uniaxial tension tests performed using different strain rates (Thiruppukuzhi and Sun 2001). The typical strain rate effect as instantaneous loading is applied on uni-directional and woven FRPs are shown in Fig. 6. Woven FRP has much larger strains at failure compared to

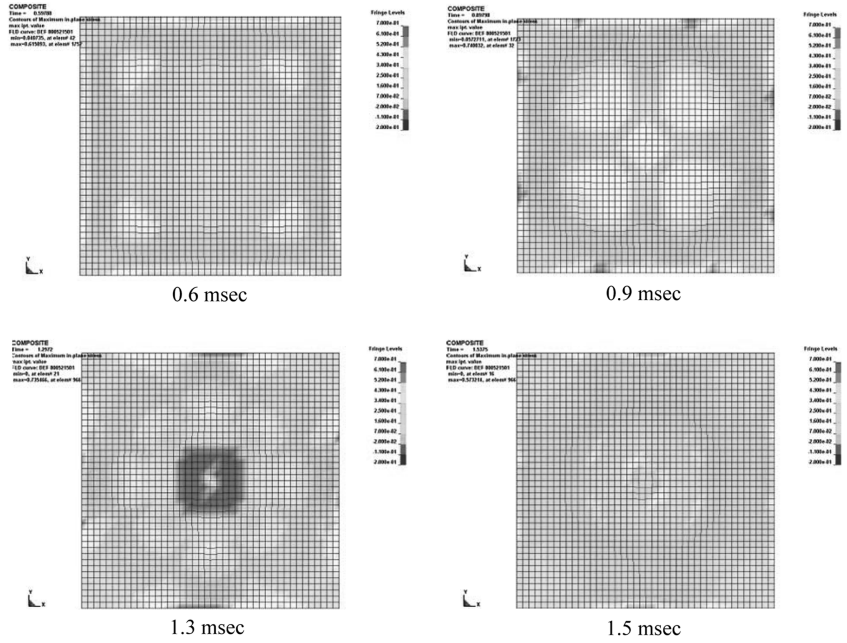

(a) Non-failure model

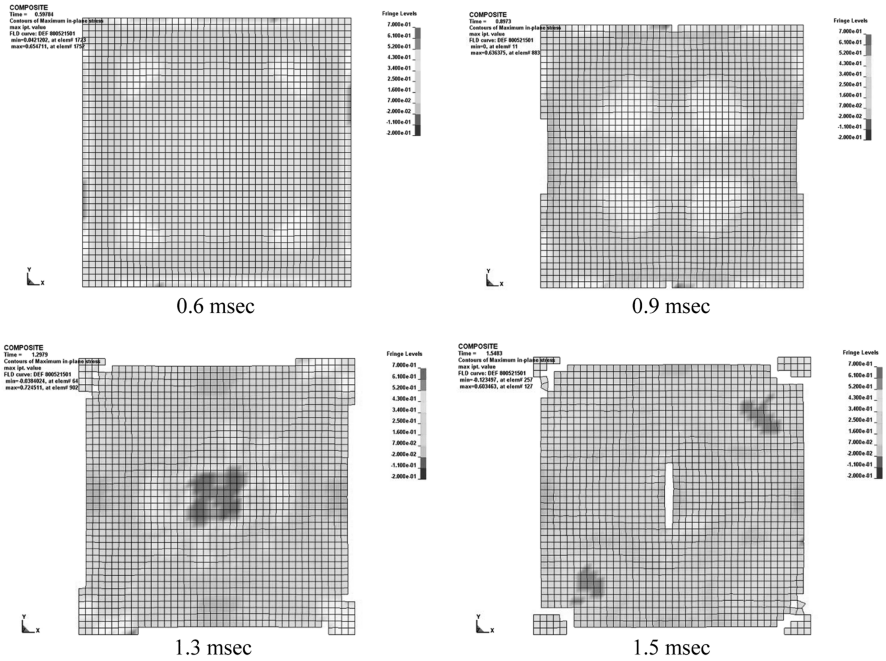

(b) Failure model

Fig. 4 Maximum in-plane stress of the non-failure model and the failure model

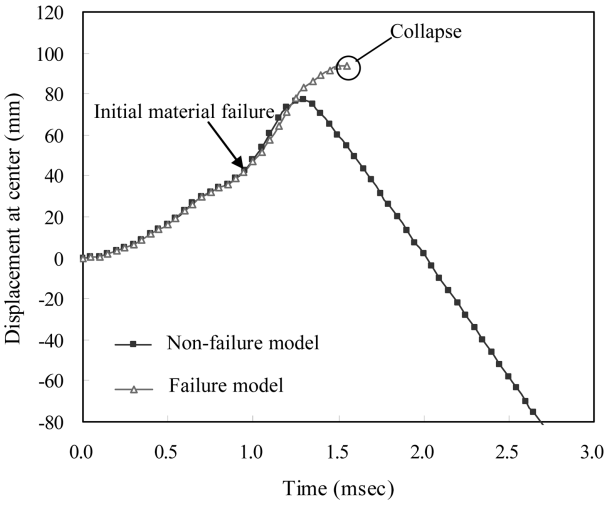

Fig. 5 Comparison of analysis results in failure and non-failure models

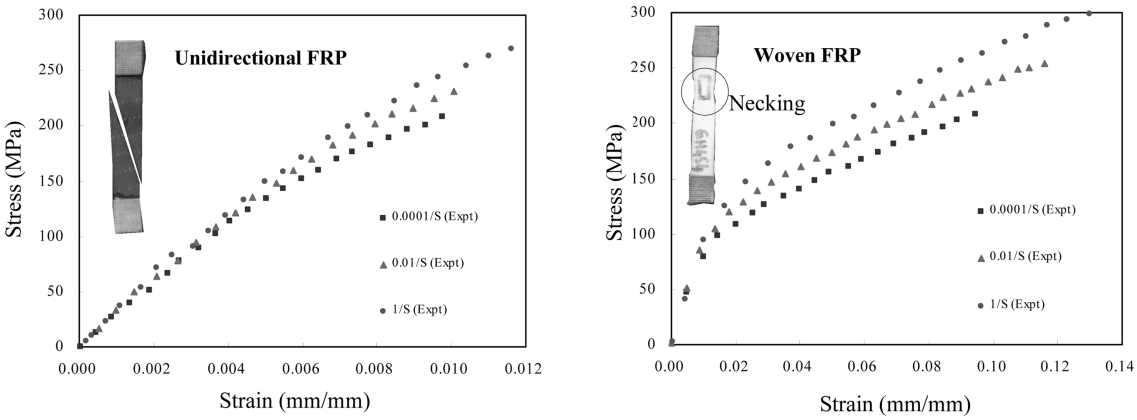

(a) Unidirectional S2-glass

(b) Woven E-glass

Fig. 6 Stress-strain curves for the off-axis specimens demonstrating rate sensitivity (Thiruppukuzhi and Sun 2001)

that of uni-directional FRP. Also, the failure mode of woven FRP is quite distinct from that of uni-directional FRP. The uni-directional FRP failure occurred along the off-axis angle parallel to the fiber direction, while the woven FRP exhibited a well-defined necking behavior before the occurrence of final failure. Therefore, the elastic-viscoplasic model based on the plastic potential function is generally used to characterize plastic deformations at a given strain rate.

Meanwhile, FRP material strengths with strain rate effect can be expressed by constitutive equation as a function of strain rate. In this study, based on Al-Hassani and Kaddour's work (1998), FRP material strengths defined as a linear function according to strain rates are proposed as shown in Eq. (9), which characterize the dynamic failure behavior.

$$X^d = X_{static} + \zeta \log \dot{\varepsilon}_{11}(\text{MPa}), \quad Y^d = Y_{static} + \xi \log \dot{\varepsilon}_{22}(\text{MPa}),$$
$$SC_{12}^d = (SC_{12})_{static} + \kappa \log \dot{\varepsilon}_{12}(\text{MPa}) \tag{9}$$

where X, Y and SC_{12} represent longitudinal, transverse, and in-plane shear strengths, respectively; ζ, ξ, κ are the material constants. Also, $\dot{\varepsilon}$ is strain rate determined from an experiment such as uniaxial tension test. Therefore, uniaxial tension test should be carried out to predict the appropriate strain rate effect on the longitudinal and shear strengths.

2.4 Analytical application and verification of the proposed rate dependent failure model

The proposed rate dependent failure model in this study is implemented in finite element analysis to confirm the strain rate effect of FRP plate. The conditions used for the strain rate effect imposed finite element analysis are as same as the previous failure model analysis as shown in Fig. 3. The plate consists of 15 plies with a lay-up sequence of 3[0, 45, 0, –45, 0]. The ply is a woven fabric made of S-2 glass fiber and SC-15 epoxy resin and its material constants are as shown in Table 2 of dynamic with strain rate effect part (Park *et al*. 2006).

The difference in the FRP behaviors according to the strain rate effect is confirmed by using the rate dependent and independent failure models as shown in Fig. 7. The rate dependent failure model uses the failure criterion enhancement during the analysis due to high strain rate effect. This result clearly confirms that the increased FRP strengths due to high strain rate effect enhance FRP blast performance. Also, it verifies that the dynamic behavior of FRP under blast load can be conservatively evaluated by the proposed rate dependent failure model. Based on the past tensile test results, material constants ζ, ξ, and κ representing strain rate effect are assigned with the value of 48.16, 48.16, and 8.08, respectively (Park *et al*. 2006).

To verify the proposed FRP rate dependent failure model, Kim and Fries's experimental data (2002) and Park *et al*.'s analytical data (2006) are used in this study as shown Fig. 8. Analytical conditions are similar to the other finite element analyses as shown in Table 2 and Fig. 3. Two

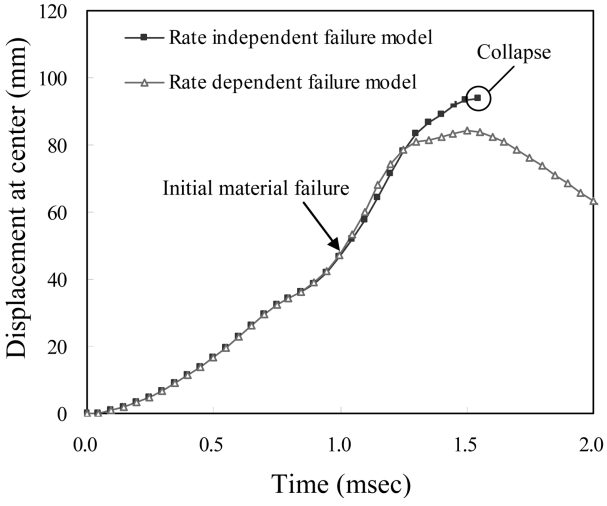

Fig. 7 Comparison of analysis results in rate-independent and -dependent failure models

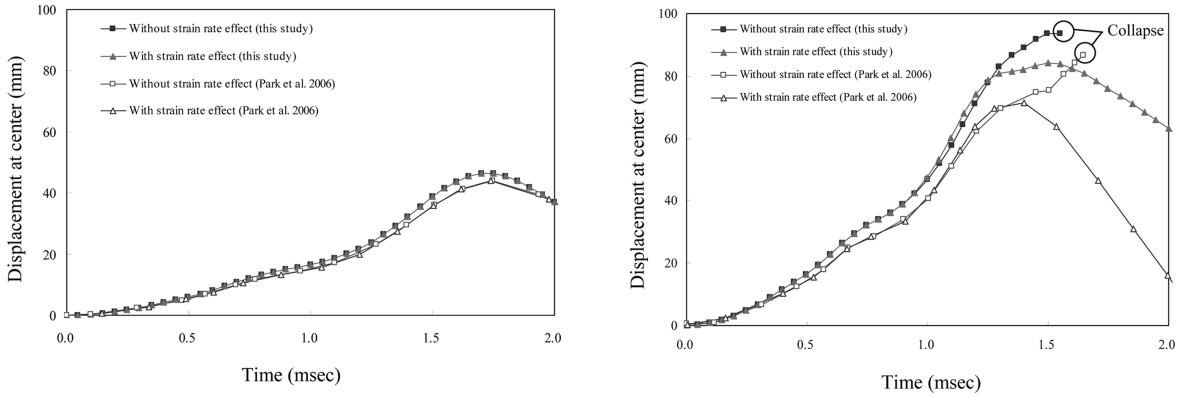

(a) Low blast pressure loading case (P_m = 1.065 MPa) (b) High blast pressure loading case (P_m = 3.100 MPa)

Fig. 8 Comparisons with past reported results of blast analysis for FRP plate

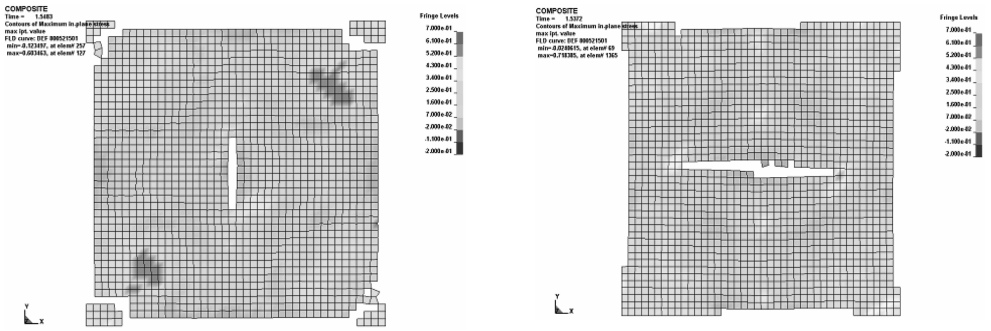

(a) Without strain-rate effect (b) With strain-rate effect

Fig. 9 Comparisons of maximum in-plane stress distribution at 1.54 msec according to rate dependency

different levels of impulse using standard TNT blast loading are applied. The blast loading is approximated as a uniform pressure over a FRP plate with the Friedlander decay function. As shown in Fig. 8(a), the calculated residual displacements from the rate independent and dependent models had no difference. This shows that the effect of strain rate on FRP material strength is negligible for low blast pressure loading P_m of 1.065 MPa. However, as shown in Fig. 8(b), the plate center displacement increased when high blast pressure loading P_m of 3.1 MPa is used. This shows that the analysis results obtained using the rate independent model erroneously predicts structural collapse by underestimating FRP material strengths. The maximum in-plane stress distribution for the analyses at the time of 1.54 msec is shown in Fig. 9. As shown in Fig. 9, the analysis results obtained using the rate independent model erroneously predicts structural collapse at approximately 1.54 msec. On the other hand, the analysis result obtained using the rate dependent model shows a local collapse at the center, which agrees well with the experimental observation as shown in Fig. 10. This comparison shows that the proposed rate dependent failure model can more accurately simulate the dynamic failure response of FRP under blast loading.

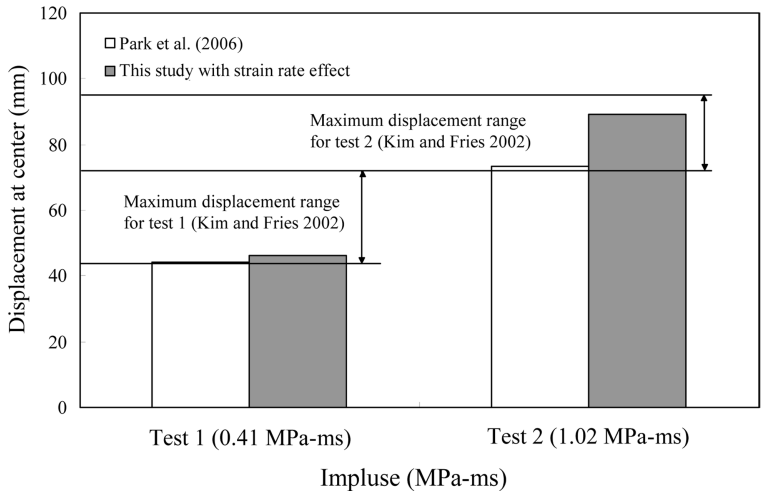

Fig. 10 Comparisons of the results between finite element analysis and the test for maximum displacement at the plate center

3. FRP debonding failure model

Debonding failure of FRP is commonly reported in blast field tests. Although numerous researches have been conducted on the bond behavior between FRP and concrete under static loading (Matta *et al*. 2005, Lenwari *et al*. 2002), only a limited number of researches have been carried out on the dynamic bond behavior; and there is still no representative bond model suitable for blast loading analysis (Buchan and Chen 2007, Shi *et al*. 2009, Li and Chen 2009, Kusumaningrum and Ong 2009). The debonding failure must be considered in a resilient retrofit design concept, because a significant portion of wave impact energy of FRP retrofitted concrete structures is dissipated by FRP debonding failure. Therefore, in this study, the impact bond behavior of FRP considering the debonding failure is modeled using the Lorenzis and Tegola's (2005) simple approach. Also, the debonding failure is implemented and simulated by contact interface modeling in finite element analysis.

3.1 Debonding failure model under static loading

The existing pull test database has shown conclusively that the failure of FRP-to-concrete bonded joint is due to cracking in concrete layer at a few millimeters distance away from adhesive layer, unless very weak adhesive or high strength concrete is used. A fracture plane propagates from a loaded end to a free end of FRP plate as load and deformation increase. From existing theoretical and experimental study results (Chen and Teng 2001, Yuan *et al*. 2004, Mahini and Ronagh 2009, Takashi 2009), main parameters governing the local bond-slip behavior and the bond strength of FRP-to-concrete bonded joints in pull tests are concrete strength, bond length L, FRP axial stiffness, FRP-to-concrete-width ratio, adhesive stiffness, and adhesive strength. A very important aspect of the behavior of the bonded joint is that an effective bond length limit L_e exists, beyond which an extension of the bond length L cannot increase the ultimate load (Lorenzis and Tegola 2005).

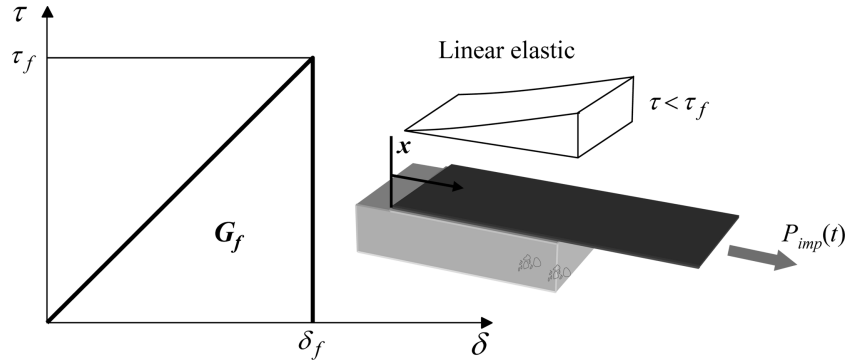

Fig. 11 Single linear bond-slip relationship (Chen and Teng 2001)

The linear bond-slip relationship is shown in Fig. 11. Since there is no interfacial softening or debonding along the FRP-to-concrete interface at a small load, the entire length of the interface can be considered to be in elastic stress state. This is true as long as the interfacial shear stress at $x = L$ is less than τ_f. For the case of $\delta \leq \delta_f$, the governing differential equation of the bond-slip relationship can be obtained as Eq. (10) (Yuan *et al*. 2001).

$$\frac{d^2\delta}{dx^2} - \lambda_1^2 \delta = 0 \tag{10}$$

where $\lambda_1^2 = \lambda^2 \frac{2G_f}{\delta_f \tau_f} = \frac{\tau_f}{\delta_f}\left(\frac{1}{E_p t_p} + \frac{b_p}{b_c E_c t_c}\right)$, $\lambda^2 = \frac{\tau_f^2}{2G_f}\left(\frac{1}{E_p t_p} + \frac{b_p}{b_c E_c t_c}\right)$ and δ_f is a slip at $\tau = \tau_f$. G_f represents interfacial fracture energy; δ_f is ultimate interfacial slip; τ_f is local bond strength; E_c and E_p represent Young's modulus of concrete and FRP, respectively; b_c, b_p, and t_p represent concrete prism width, FRP bonded width, and FRP thickness, respectively.

The expressions for interfacial slip, interfacial shear stress, and axial stress in FRP are given by Eqs. (11)-(13), respectively, by solving Eq. (10).

$$\delta = \frac{\delta_f}{\tau_f} \frac{P\lambda_1 \cosh(\lambda_1 x)}{b_p \sinh(\lambda_1 L)} \tag{11}$$

$$\tau = \frac{P\lambda_1 \cosh(\lambda_1 x)}{b_p \sinh(\lambda_1 L)} \tag{12}$$

$$\sigma_p = \frac{P \sinh(\lambda_1 x)}{b_p t_p \sinh(\lambda_1 L)} \tag{13}$$

where P is a maximum load in pull-test.

3.2 Debonding failure model under blast loading

In this section, dynamic FRP debonding failure model for the evaluation of bond strength of FRP under blast loading is developed. Also, to improve analysis effectiveness, the simple model of Lorenzis and Tegola (2005) for the debonding failure model of FRP to concrete under blast loading

is formulated based on bond interface material properties as a function of the ratio of dynamic to static bond strengths.

The bond interface relationship between FRP and concrete is assumed as a linear bond-slip relationship and an FRP-concrete bonded joint of an unit width and a length of $L >> L_e$ is assumed to be subjected to an impulse load $P_{imp}(t)$ as shown Fig. 11. The impulse load increment corresponding to a time t during FRP interface operation time t_a can be expressed as Eq. (14). To prevent divergence of bond strength, assumption of minimum length $s_{\min}$ is adopted as a parameter. The function of bond strength increment as a function of a load increment can be obtained using mechanical assumptions and mathematical operations as shown in Eqs. (15) and (16).

$$dP_{imp} = (dP_{imp}/dt)dt = P'_{imp}(t)dt \tag{14}$$

$$\tau_{le}(t_a) = \tau_{\max} = \frac{2}{L_e}\coth\left(\frac{2s_{\min}}{L_e}\right)[P(t_a)-P(0)] = \frac{2}{L_e}\coth\left(\frac{2s_{\min}}{L_e}\right)P_{\max}, \text{ if } \frac{t_a}{t_e} \le \frac{s_{\min}}{L_e} \tag{15}$$

$$\tau_{le}(t_a) = \tau_{\max} = \frac{2}{L_e}\int_0^{t_{\max}}\left\{P(t)\coth\left(\frac{2(t_a-t)}{t_e}\right)dt + \frac{2}{L_e}\coth\left(\frac{2s_{\min}}{L_e}\right)\times\left[P_{\max}-P\left(t_a-\frac{s_{\min}}{L_e}t_e\right)\right]\right\}$$

$$\text{if } \frac{s_{\min}}{L_e} \le \frac{t_a}{t_e} \le \frac{L}{L_e} \tag{16}$$

where τ_{le} is bond stress at the loaded end. t_a and t_e represent a total time duration of blast loading and time duration needed for a longitudinal wave to travel a length equal to the effective bond length, respectively.

Meanwhile, the bond strength ratio relationship between static and dynamic bond strengths can be expressed as Eq. (17), which is a well-known Friedlander decay function. From a structural point of view, a blast impulse is more of an influencing factor than a maximum blast pressure for response or damage of structural components. Generally, the impulse-time curve can be obtained by the integration of the blast pressure-time curve as shown in Fig. 12. This study evaluates the bond strength under blast loading using a blast impulse-time history, which is obtained by integrating of the blast pressure-time history based on the Friedlander decay function. The blast impulse-time history function is expressed as Eq. (18).

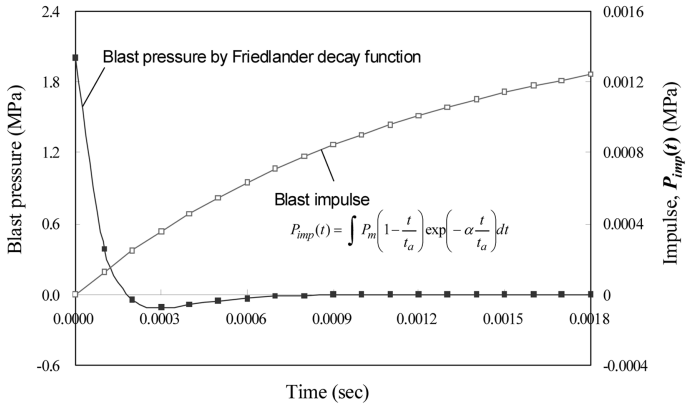

Fig. 12 Relationship of blast pressure- and impulse-time histories

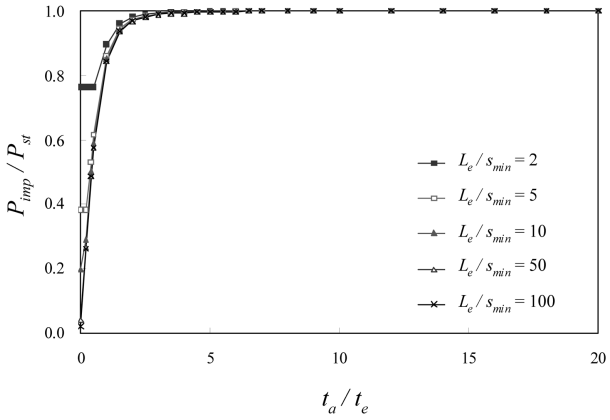

Fig. 13 Ratio of the bond failure load of blast loading and static cases (Nam *et al*. 2010)

$$\tau_{\max}^{st}/\tau_{\max}^{imp} = P_{imp}/P_{st} = S_d \tag{17}$$

$$P_{imp}(t) = \int_0^t \left\{ P_m\left(1-\frac{t}{t_a}\right)\exp\left(-\alpha\frac{t}{t_a}\right)\right\}dt = P_m\frac{t_a}{\alpha}\left[1+e^{-\alpha\frac{t}{t_a}}\left(-1+\frac{t}{t_a}\right)+\frac{1}{\alpha}\left(e^{-\alpha\frac{t}{t_a}}-1\right)\right] \tag{18}$$

The ratio of the bond strengths under static and blast cases can be derived as Eq. (19) from Eqs. (17) and (18).

$$\tau_{\max}^{st}/\tau_{\max} = \left(1-\frac{1}{\alpha}+\frac{1}{\alpha}e^{-\alpha}\right)/\left\{\int_0^b me^{-\alpha t}dt+\frac{1}{\alpha}\coth\left(\frac{2s_{min}}{L_e}\right)\left[e^{-\alpha}-ne^{-\alpha\left(1-\frac{s_{\min}}{L_e}\frac{t_e}{t_p}\right)}\right]\right\} \tag{19}$$

Where $b = 1-\frac{s_{\min}}{L_e}\frac{t_e}{t_p}$, $m = \alpha(1-t)\coth\left(\frac{2t_p(1-t)}{t_e}\right)$, $n = \left(1-\alpha\frac{s_{\min}}{L_e}\frac{t_e}{t_p}\right)$; $\tau_{\max}^{st}$ and $\tau_{\max}^{imp}$ represent the maximum bond stresses of the bonded joint under static and impulse loading cases, respectively; P_{st} and P_{imp} are tensile forces applied to a joint, which produce local bond strength τ_f at the loaded end under static and blast loading cases, respectively; S_d is a dynamic interfacial strength conversion factor; m, n are the experimental constants.

From the above approach, the calculated ratio of the bond failure load of the FRP-concrete bonded joint under a blast to static case is shown in Fig. 13. A trend can be observed from Fig. 13 where the blast impulse may produce a substantial reduction of the debonding load compared to the static case; and this reduction is more significant for a larger $L_e/s_{\min}$ ratio (i.e., when the minimum activated length of the joint is shorter).

3.3 Implementation of the debonding failure model

Since analytical implementation of the debonding model is still difficult, the aim is to develop finite element simulation to enable structural evaluation of FRP debonding failure under blast loading. Three-dimensional modeling and analysis of the interface between FRP and concrete connected by an appropriate bonding condition can be seen as the most accurate way of simulating the debonding failure. The contact breakage command "CONTACT_AUTOMATIC_SURFACE_

TO_SURFACE_TIEBREAK" in LS-DYNA is invoked to model the interface between FRP and concrete. This contact algorithm uses a penalty method to model the contact interface between the different parts or materials. Therefore, the failure parameters can easily be adapted to the actual behavior by choosing an appropriate adhesive material model to separate the attached surface between FRP and concrete to simulate debonding. Reaching the failure threshold, the elements are deleted to eliminate numerical instabilities due to the complex internal energy algorithms and the mass loss from the stress-based debonding failure criteria defined as follows.

$$\left(\frac{\sigma_n}{R_n}\right)^2+\left(\frac{\sigma_s}{R_s}\right)^2=1 \quad \text{for} \quad \sigma_n>0\,, \quad \left(\frac{\sigma_n}{S_d R_n}\right)^2+\left(\frac{\sigma_s}{S_d R_s}\right)^2=\left(\frac{\sigma_n}{R_n^d}\right)^2+\left(\frac{\sigma_s}{R_s^d}\right)^2=1 \quad \text{for} \quad \sigma_n>0 \tag{20}$$

where σ_n and σ_s denote normal and shear stresses components, respectively. R_n and R_s are corresponding normal and shear failure stresses, respectively; S_d is dynamic strength conversion factor, which can be obtained by using proposed approach for bond strength under blast loading.

4. Debonding failure analysis under blast loading

To evaluate the effect of the debonding failure, this study carried out additional finite element analysis using the dynamic bond strength model. The simulated structure is a RC beam with 400 mm width, 100 mm height, and 1,100 mm length as shown in Fig. 14. The main objective of this analysis is to show the difference between perfect bonding and debonding failure models. Therefore, an arbitrary dynamic load is applied to induce debonding failure. The adhesive interface of FRP to concrete is applied using the contact interface model, which is implemented by the contact algorithm mentioned previously. The interfacial bond strength is expressed as the debonding failure criterion in this study and is based on shear and normal stresses in the interface.

The comparative analysis results of the perfect bonding and debonding failure models are shown in Fig. 15. The localized material and debonding failures are initiated at 40 msec from the initiation of loading in the case of the debonding failure model. However, using the perfect bonding model,

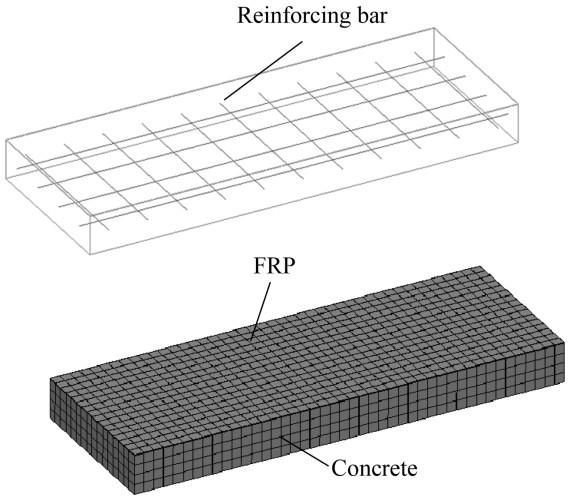

Fig. 14 Finite element models of concrete, reinforcing bar, and FRP

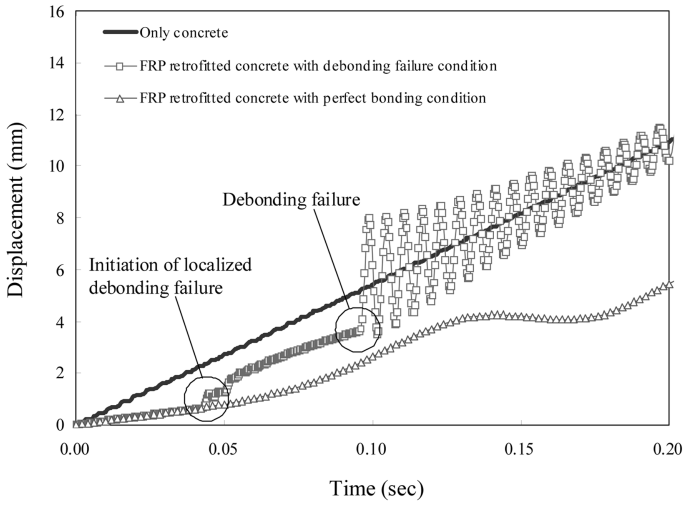

Fig. 15 Difference of analysis results according to FRP retrofit conditions

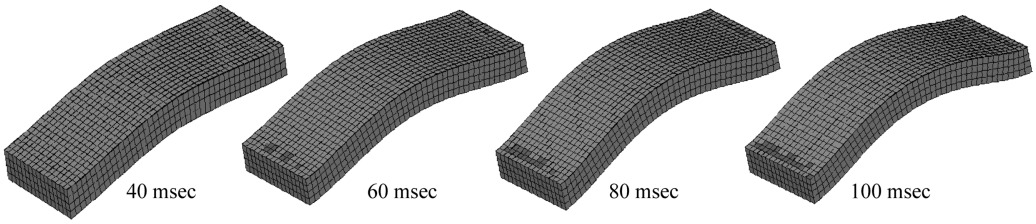

(a) Perfect bonding model

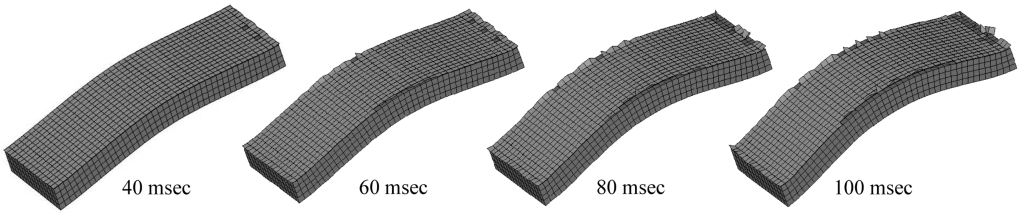

(b) Debonding failure model

Fig. 16 Comparison of the analysis results of the perfect bond and debonding failure models

some material failure occurred, but there was no occurrence of debonding failure. The FRP simulation results obtained with the debonding failure model is totally different than that with the perfect bonding model. The comparison result obviously shows that the proposed debonding model is necessary to accurately simulate FRP-retrofitted concrete structural behavior. Also, a graphic comparison of the analysis results of FRP-retrofitted concrete beam with the perfect bonding and debonding is shown in Fig. 16. In case of the perfect bonding model, the FRP elements violating the FRP bonding criterion are deleted, which are represented by the transparent locations on the top surface. However, in case of the debonding failure model, the interfacial contact elements violating

the bond failure criterion are eliminate, which are represented by the peeled-off edge locations in the top surface. Fig. 16 obviously shows that the proposed debonding model can better simulate the debonding failure of an FRP retrofitted concrete structure.

5. Blast analysis of FRP-retrofitted concrete structure

To evaluate the overall structural effect from the debonding failure, a simulation on the blast field test performed by Razaqpur *et al*. (2007) and Tolba (2001) is carried out. As shown in Fig. 17, the blast test was performed on a GFRP-retrofitted two-way RC panel with dimensions of 1,000 × 1,000 × 70 mm. The reinforcement yield and ultimate strengths are 480 MPa and 600 MPa, respectively. Concrete with an average 28-day compressive strength of 40 MPa and an average compressive strength just prior to the blast testing of 42 MPa was used to cast the specimens. The panel were retrofitted on both top and bottom faces with two laminates of GFRP arranged in a crucifix form with laminates parallel to the edges of the panel as shown in Fig. 17. Each GFRP laminate was 500 mm wide, covering the middle half of the panel. The explosive used for the test was approximately 33.4 kg of ANFO, which is equivalent to 27.4 kg of TNT using a conversion factor of 0.82 with 3.0 m standoff distance from the center of the charge to the center of the test panel.

The finite element model with loading and boundary conditions for this blast simulation is shown in Fig. 18. The adhesive interface of FRP to concrete is implemented into the model by the contact algorithm in LS-DYNA. Table 3 shows the material properties used in the blast simulation, which are same as those from the experimental report. The rate dependent failure models as well as the proposed debonding failure model of GFRP are used. For the strain rate effect, the failure criteria as a function of strengths are used.

The simulation results obtained using the proposed debonding and rate dependent failure models show good agreement with the experimental results as shown in Fig. 19. Razaqpur *et al*. (2007)

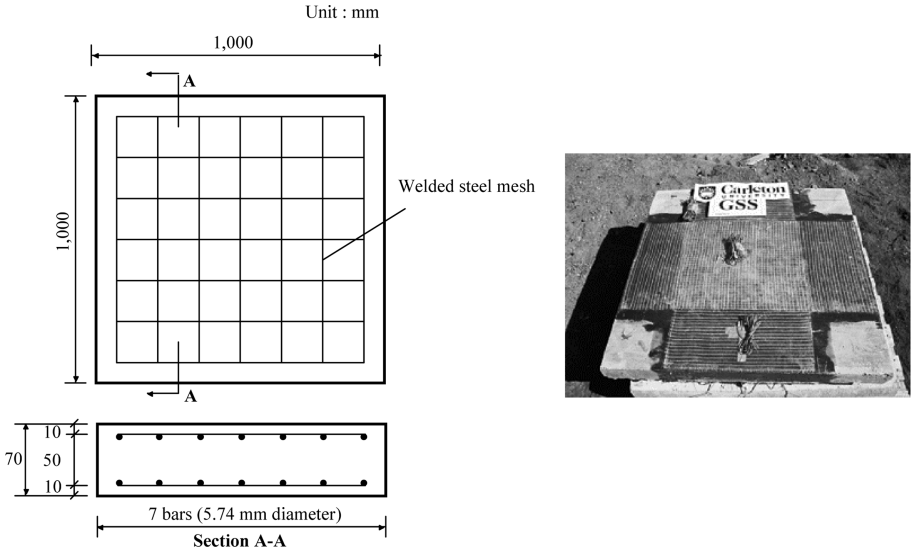

Fig. 17 Test specimen geometry and GFRP-retrofitted RC panel (Razaqpur *et al*. 2007)

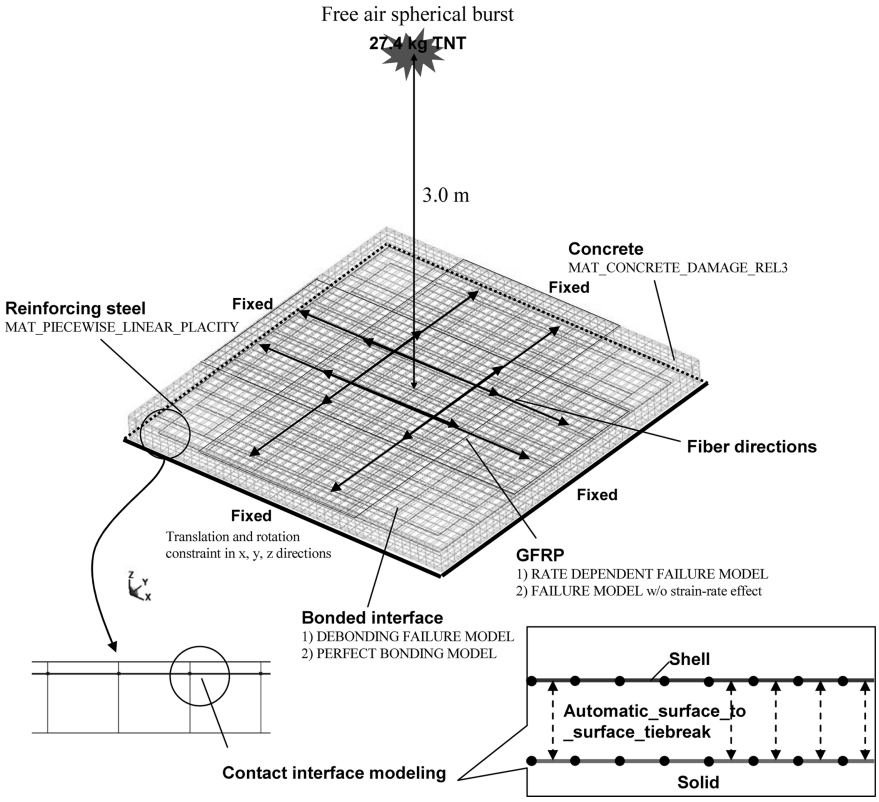

Fig. 18 Finite element model with loading and boundary conditions

Table 3 Material properties used in blast analysis (Nam *et al*. 2010)

	Material properties	Value
Concrete	Compressive strength (MPa)	42
	Tensile strength (MPa)	4.0
	Young's modulus (GPa)	29
	Poisson's ratio	0.167
Reinforcing steel	Yield strength (MPa)	480
	Ultimate strength (MPa)	600
GFRP	Longitudinal modulus E_x (GPa)	27.5
	Transverse modulus E_y (GPa)	1.3
	Shear modulus G_{xy} (GPa)	0.27
	Poisson's ratio ν_{xy}	0.23
	Longitudinal tensile strength X_t (MPa)	$410.2\log\dot{\varepsilon}_{11}+459.2$
	Longitudinal compressive strength X_c (MPa)	318.0
	Transverse tensile strength Y_t (MPa)	$146.5\log\dot{\varepsilon}_{22}+17.2$
	Transverse compressive strength Y_c (MPa)	10.5
	In-plane shear strength SC (MPa)	$6.2\log\dot{\varepsilon}_{12}+7.9$
	Density ρ (kg/m^3)	2,100

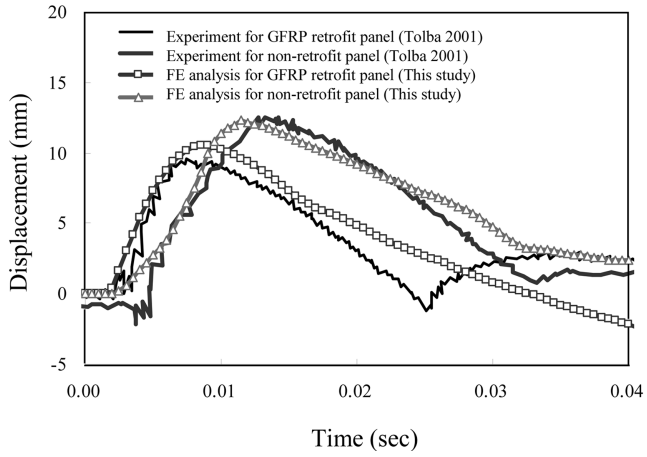

Fig. 19 Comparison of test and analysis results (Nam *et al*. 2010)

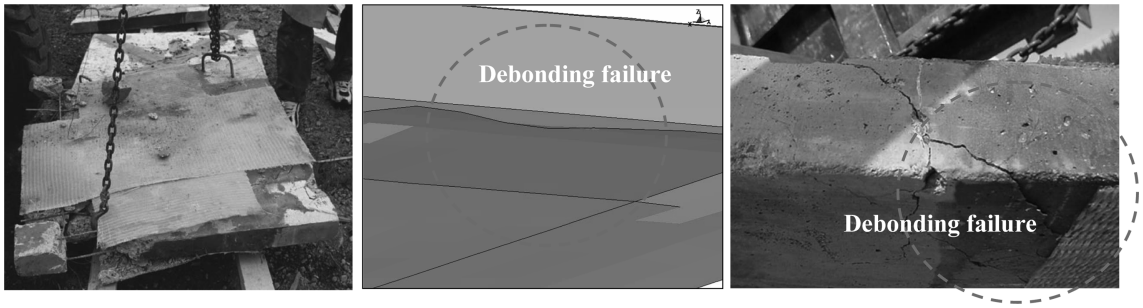

Fig. 20 Analytical prediction of the local debonding failure (Nam *et al*. 2010)

reported that inherent variabilities exist in blast field tests such as atmospheric pressure, temperature, humidity, wind, etc. Therefore, even under exactly same testing conditions, different data can be obtained. With this inherent variabilities in mind, simulation results agree relatively well with the experimental measurements of the overall structural displacement behavior of the RC panel under the same explosive charge loading and testing conditions. Especially, the results confirm that much more accurate simulation of the failure behavior of FRP retrofitted RC panel is possible using the proposed local debonding FRP failure model as shown in Fig. 20.

6. Conclusions

This study suggests an enhanced blast analysis technique that considers the rate-dependent failure criteria and debonding failure mechanisms of a FRP-retrofitted concrete structure subjected to blast loading. The conclusions from the study are as follows.

1) In order to consider the realistic failure mechanisms, the strain rate effect need to be considered in the FRP failure criteria. From the simulation results obtained from finite element analysis using the developed rate dependent failure model, it is confirmed that an accurate simulation of the realistic failure behaviors of FRP under blast loading is possible.

2) The local debonding failure mechanism of FRP, commonly reported in blast field test results, is achieved in the simulation by incorporating new debonding failure model. To evaluate the dynamic bond behavior of the interface between concrete and FRP under blast loading, a new debonding model is developed by incorporating the Friedlander decay function into the Lorenzis and Tegola's simple dynamic bond behavior model. The newly developed debonding failure model is used to obtain accurate and realistic simulation results.

3) Using the proposed dynamic model in the finite element analysis as a contact interface model, the blast simulation results of GFRP retrofitted RC panel confirms that the debonding failure of FRP can reasonably simulate FRP local debonding and overall structural failure behaviors.

Acknowledgements

This study was supported by the Nuclear Research & Development of the Korea institute of Energy Technology Evaluation and Planning (KETEP) grant funded by the Korea government Ministry of Knowledge Economy (Grant No.: 2010-1620100180) and Gas Plant R&D Center funded by the Ministry of Land, Transportation and Maritime Affairs (MLTM) of the Korean government (Grant No.: 2010-8-0988).

References

Al-Hassini, S.T.S. and Kaddour, A.S. (1998), "Strain rate effect on GRP, KRP and CFRP composite laminates", *Key Eng. Mat*., **141-143**(Pt2), 427-452.

Al-Salehi, F.A.R., Al-Hassani, S.T.S. and Hinton, M.J. (1989), "An experimental investigation into the strength of angle ply GRP tubes under high rate of loading", *J. Comput. Mat.*, **23**(3) 288-305.

Buchan, P.A. and Chen, J.F. (2007), "Blast resistance of FRP composite and polymer strengthened concrete and masonry structures-A State-of-the-Art Review", *Compos. Part B-Eng*., **38**(5-6), 509-522.

Chang, F.K. and Chang, K.Y. (1987), "A progressive damage model for laminated composite containing stress concentration", *J. Compos. Mater*., **21**(9), 834-855.

Chen, J.F. and Teng, J.G. (2001), "Anchorage strength models for FRP and steel plates bonded to concrete", *J. Struct. Eng.-ASCE*, **127**(7), 784-791.

Cho, J.U. (2009), "Evaluation of critical impact energy on aluminum foam using numerical and experimental analysis", *Proceeding of Computational Design in Engineering (CODE 2009)*, Seoul, Korea, November.

Dai, J., Harries, K.A. and Yokota, H. (2008), "A critical steel yielding length model for predicting intermediate crack-induced debonding in FRP strengthened RC members", *Steel Compos. Struct*., **8**(6), 457-473.

Dai, J.G., Harries, K.A. and Yokota, H. (2008), "A critical steel yielding length model for predicting intermediate crack-induced debonding in FRP-strengthened RC members", *Steel Compos. Struct*., **8**(6), 457-473.

Dancygier, A.N. (2009), "Characteristics of high performance reinforced concrete barriers that resist non-deforming projectile impact", *Struct. Eng. Mech*., **32**(5), 685-699.

Davidson, J.S., Fisher, J.W., Hammons, M.I., Porter, J.R. and Dinan, R.J. (2005), "Failure mechanisms of polymer-reinforced concrete masonry walls subjected to blast", *J. Struct. Eng.-ASCE*, **131**(8), 1194-1205.

Dogan, A.B. and Anil, O. (2010), "Nonlinear finite element analysis of effective CFRP bonding length and strain distribution along concrete-CFRP interface", *Comput. Concrete*, **7**(5), 437-453.

Gibson, R.F. (1994), *Principles of Composite Material Mechanics*, McGraw-Hill, New York.

Gong, S.F., Lu, Y., Tu, Z. and Jin, W. (2009), "Validation study on numerical simulation of RC response to close-in blast with a fully coupled model", *Struct. Eng. Mech*., **32**(2), 269-282.

Guzas, E.L. and Earls, C.J. (2010), "Air blast load generation for simulating structural response", *Steel Compos. Struct*., **10**(5), 429-455.

Hashin, Z. (1980), "Failure criteria for unidirectional fiber composite", *ASME J. Appl. Mech*., **47**(2), 329-334.
Kim, K. and Fries, J. (2002), "Blast response of glass-fiber composite plates with progressive material damage model", *Proceedings of the 73rd Shock and Vibration Symposium*, Newport, Rhode Island, November.
Kollar, L.P. and Springer, G.S. (2002), *Mechanics of Composite Structures*, Cambridge University Press, UK.
Kotsovos, M.D., Pavlovic, M.N. and Cotsovos, D.M. (2008), "Characteristic features of concrete behaviour: Implications for the development of an engineering finite-element tool", *Comput. Concrete*, **5**(3), 243-260.
Kumar, S. (2010), "Analysis of impact response and damage in laminated composite cylindrical shells undergoing large deformations", *Struct. Eng. Mech*., **35**(3), 349-364.
Kusumaningrum, P. and Ong, K.C.G. (2009), "Performance of RC columns retrofitted with hybrid-fiber ECC subjected to blast loading", *Proceeding of Computational Design in Engineering (CODE 2009)*, Seoul, Korea, November.
Landry, K.A. (2003), "The blast resistance of unreinforced, ungrouted, one-way, concrete masonry unit walls", Thesis of Doctor of Philosophy, Rensselaer Polytechnic Institute Troy, New York, USA.
Lenwari, A., Thepchatri, T. and Watanabe, E. (2002), "Prediction of premature separation of bonded CFRP plates from strengthened steel beams using a fracture criterion", *Struct. Eng. Mech*., **14**(5), 565-574.
Li, G.Q., Yang, T.C. and Chen, S.W. (2009), "Behavior and simplified analysis of steel-concrete composite beams subjected to localized blast loading", *Struct. Eng. Mech*., **32**(2), 337-350.
Lorenzis, L.D. and Tegola, A.L. (2005), "Bond of FRP laminates to concrete under impulse loading : A simple model", *Proceedings of the International Symposium on Bond Behaviour of FRP in Structures (BBFS 2005)*, Hong Kong, December.
Lu, Y. (2009), "Modelling of concrete structures subjected to shock and blast loading: An overview and some recent studies", *Struct. Eng. Mech*., **32**(2), 235-249.
Mahini, S.S. and Ronagh, H.R. (2009), "Numerical modelling of FRP strengthened RC beam-column joints", *Struct. Eng. Mech*., **32**(6), 649-665.
Malvar, L.J., Crawford, J.E., Wesevich, J.W. and Simons, D. (1997), "A plasticity concrete material model for DYNA3D", *Int. J. Impact Eng*., **19**(9-10), 847-873.
Malvar, L.J., Morrill, K.B. and Crawford, J.E. (2004), "Numerical modeling of concrete confined by fiber reinforced composites", *J. Compos. Constr*., **8**(4), 315-322.
Matta, F., Karbhari V.M. and Vitaliania, R. (2005), "Tensile response of steel/CFRP adhesive bonds for the rehabilitation of civil structures", *Struct. Eng. Mech*., **20**(5), 589-608.
Morrill, K.B., Malvar, L.J., Crawford, J.E., Hegemier, G. and Seible, F. (2001), "Full-scale testing of reinforced concrete column retrofits to resist blast loads", *Proceedings of 10th International Symposium on Interaction of the Effects of Munitions with Structures*, Defense Threat Reduction Agency, San Diego.
Nam J.W., Kim, H.J., Yi, N.H., Kim, I.S., Kim, J.H.J. and Choi, H.J. (2009), "Blast analysis of concrete arch structures for FRP retrofitting design", *Comput. Concrete*, **6**(4), 305-318.
Nam, J.W., Kim, H.J. Kim, S.B., Yi, N.H. and Kim, J.H.J. (2010), "Numerical evaluation of the retrofit effectiveness for GFRP retrofitted concrete slab subjected to blast pressure", *Compos. Struct*., **92**(5), 1212-1222.
Nam, J.W., Kim, H.J., Kim, S.B., Kim, J.H.J. and Byun, K.J. (2009), "Analytical study of finite element models for FRP retrofitted concrete structure under blast loads", *Int. J. Damage Mech*., **18**(5), 461-490.
Ngo, T. and Mendis, P. (2009), "Modelling the dynamic response and failure modes of reinforced concrete structures subjected to blast and impact loading", *Struct. Eng. Mech.*, **32**(2), 269-282.
Pandey, A.K. (2010), "Damage prediction of RC containment shell under impact and blast loading", *Struct. Eng. Mech*., **36**(6), 729-744.
Park, H. (2003), "A nonlinear solid shell element formulation for analysis of composite panels under blast wave pressure loading", Thesis of Doctor of Philosophy, University of Maryland, Maryland, USA.
Park, H., Lee, K., Lee, S.W. and Kim, K. (2006), "Dynamic analysis of nonlinear composite structures under pressure wave loading", *J. Compos. Mater*., **40**(15), 1361-1383.
Pham, D.H. (2002), Finite Element Study of a Composite Tube under Impact Load, SAE 2002 World Congress Technical Paper 2002-01-0723, Detroit, Michigan, March.
Razaqpur, A.G., Tolba, A. and Contestabile, E. (2007), "Blast loading response of reinforced concrete panels reinforced with externally bonded GFRP laminates", *Compos. Part B-Eng*., **38**(5-6), 535-546.

Shi, Y., Li, Z.X. and Hao, H. (2009), "Bond slip modelling and its effect on numerical analysis of blast-induced responses of RC columns", *Struct. Eng. Mech*., **32**(2), 251-267.
Swanson, S.R. (1997), *Advanced Composite Materials*, Prentice-Hill, Upper Saddle River, New Jersey.
Takashi, H. (2009), "Analysis and design of FRP dome structure", *Proceeding of Computational Design in Engineering (CODE 2009)*, Seoul, Korea, November.
Thiruppukuzhi, S.V. and Sun, C.T. (2001), "Models for the strain-rate dependent behavior of polymer composites", *Comp. Sci. Tech*., **61**, 1-12.
Tolba, A. (2001), Response of FRP-Retrofitted Reinforced Concrete Panels to Blast Loading, Thesis of Doctor of Philosophy, Department of Civil and Environmental Engineering, Carleton University, Ottawa, Canada, December.
Valipour, H.B., Huynh, L. and Foster, S.J. (2009), "Analysis of RC beams subjected to shock loading using a modified fibre element formulation", *Comput. Concrete*, **6**(5), 377-390.
Yi, N.H., Lee, J.G., Kim, S.B., Kim, J.H.J. and Kim, H.J. (2009), "Blast analysis of FRP-retrofitted concrete slab considering rate-dependent failure", *Proceeding of Computational Design in Engineering (CODE 2009)*, Seoul, Korea, November.
Yuan, H., Teng, J.G., Seracino, R., Wu, Z.S. and Yao, J. (2004), "Full-range behavior of FRP-to-concrete bonded joints", *Eng. Struct*., **26**(5), 553-564.
Yuan, H., Wu, Z.S. and Yoshizawa, H. (2001), "Theoretical solutions on interfacial stress transfer of externally bonded steel/composite laminates", *J. Struct. Mech. Earthq. Eng.-JSCE*, **38**(1), 27-39.
Yun, G.J., Harmon, T.G., Dyke, S.J. and So, M. (2008), "A total strain-based hysteretic material model for reinforced concrete structures: theory and verifications", *Comput. Concrete*, **5**(3), 217-241.
Zhou, X.T., Ko, J.M. and Ni, Y.Q. (2007), "Experimental study on identification of stiffness change in a concrete frame experiencing damage and retrofit", *Struct. Eng. Mech*., **25**(1), 39-52.